In Situ Grown AgI/Bi$_{12}$O$_{17}$Cl$_2$ Heterojunction Photocatalysts for Visible Light Degradation of Sulfamethazine: Efficiency, Pathway, and Mechanism

Chengyun Zhou,[†,‡] Cui Lai,[†,‡] Piao Xu,[†,‡] Guangming Zeng,*[,†,‡] Danlian Huang,*[,†,‡] Chen Zhang,[†,‡] Min Cheng,[†,‡] Liang Hu,[†,‡] Jia Wan,[†,‡] Yang Liu,[†,‡] Weiping Xiong,[†,‡] Yaocheng Deng,[†,‡] and Ming Wen[†,‡]

[†]College of Environmental Science and Engineering, Hunan University, 8 South Lushan Road, Yuelu District, Changsha 410082, P.R. China

[‡]Key Laboratory of Environmental Biology and Pollution Control, Ministry of Education, Hunan University, 8 South Lushan Road, Yuelu District, Changsha 410082, P.R. China

Ⓢ Supporting Information

ABSTRACT: Visible-light-driven photocatalysts attract great interest because they can utilize more sunlight for reactions than conventional photocatalysts. A novel visible-light-driven photocatalyst AgI/Bismuth oxychloride (Bi$_{12}$O$_{17}$Cl$_2$) hybrid was synthesized by a hydrothermal-precipitation method. Several characterization tools, such as X-ray powder diffraction (XRD), scanning electron microscopy (SEM), high-resolution transmission electron microscopy (HRTEM), X-ray photoelectron spectroscopy (XPS), and UV−vis diffuse reflectance spectroscopy (DRS) were employed to study the phase structures, morphologies, and optical properties of the fabricated photocatalysts. These characterizations indicated that AgI nanoparticles were evenly distributed on the surface of Bi$_{12}$O$_{17}$Cl$_2$, and heterostructures were formed. The photochemical characterizations demonstrated that the promoted separation of carrier transfer in the AgI/Bi$_{12}$O$_{17}$Cl$_2$ heterojunction was achieved. The degradation rate of sulfamethazine (SMZ) by AgI/Bi$_{12}$O$_{17}$Cl$_2$ was about 7.8 times and 35.2 times higher than that of pristine Bi$_{12}$O$_{17}$Cl$_2$ and BiOCl under visible-light-driven photocatalysts, respectively. It was also found that the amount of AgI in the AgI/Bi$_{12}$O$_{17}$Cl$_2$ composites played an important role in photocatalytic activity, and the optimized ratio was 25%. The AgI/Bi$_{12}$O$_{17}$Cl$_2$ shows good catalytic stability and maintains similar reactivity after four cycles. Furthermore, the degradation intermediates of SMZ were identified by HPLC-MS, and the photocatalytic mechanism was proposed. These findings highlight the role of Bi$_{12}$O$_{17}$Cl$_2$ on contaminant elimination and open avenues for the rational design of highly efficient photocatalysts.

KEYWORDS: AgI/Bi$_{12}$O$_{17}$Cl$_2$, Photocatalytic degradation, Sulfamethazine wastewater, Heterojunctions
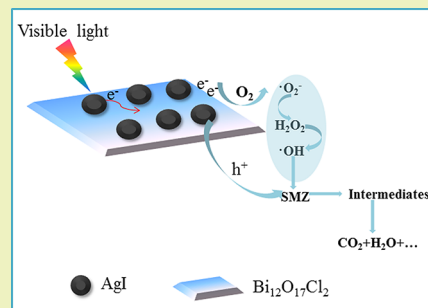
INTRODUCTION

Chemicals such as pharmaceuticals (e.g., antibiotics, antidepressants, analgesics) and personal care products (e.g., shampoos, hair dyes, and soaps) have caused a new water quality issue.[1−6] Recently, sulfonamide antibiotics were classified as a priority risk group due to their high toxicity to bacteria at low concentrations, combined with their potential to cause resistance among natural bacterial populations.[7−9] Many studies found that a conventional wastewater treatment plant can only partially remove antibiotics (20−90%).[10] A number of physical adsorption,[11−16] chemical reactions,[17−20] and biological degradation[21,22] methods have been applied to remove contaminants in wastewater. Pollutants can be migrated by physical adsorption but cannot be completely eliminated. Biodegradation usually takes a long period of time and is often used to treat low concentrations of contaminants. Chemical reaction outcomes can also be considered as contaminants.[23]

There is even some evidence that these degradation products can be as active and/or toxic as their parent.[24]

In response to the increasing pollution issues, semiconductor photocatalysis as a green technology has garnered particular attention. A lot of photocatalysts like TiO$_2$,[25,26] g-C$_3$N$_4$,[27,28] CdS,[29] and SrTiO$_3$[30] were explored for photocatalysis. Recently, bismuth-based materials are widely applied for the degradation of pollutant and water splitting.[31] Bismuth oxychloride (BiOCl), a wide band gap (about 3.3 eV) photocatalyst, has recently attracted considerable attention due to its good activity.[32−34] Especially, the layered structure feature of BiOCl can promote the effective separation of the photoinduced electron−hole pairs, which is an important factor for photocatalysis.[35,36] The BiOCl photocatalyst exhibited high

activity on pollutant degradation under UV light. Zhang has explored facet-controllable BiOCl, which offered superior activity on indirect dye photosensitization degradation under visible light.[37] Although many achievements have been reported, it is difficult to further narrow the band gap of BiOCl. Therefore, the strategy to reduce the band gap still needs to be explored.

Density functional theory (DFT) calculations suggest that an effective measure to decrease the band gap is to change the relative atomic ratios of BiOCl, such as $Bi_{12}O_{17}Cl_2$.[38−42] $Bi_{12}O_{17}Cl_2$ has the nanosheet structure with $Bi_{12}O_{17}^{2+}$ and $Cl_2^{2−}$ layers.[43] With a relative small band gap (2.2−2.4 eV), $Bi_{12}O_{17}Cl_2$ can absorb visible light and be applied to degraded organic contaminants in water.[44] Nevertheless, the photocatalytic activity of $Bi_{12}O_{17}Cl_2$ is limited due to the high recombination rate of the photogenerated electron−hole pairs. Coupling $Bi_{12}O_{17}Cl_2$ with other semiconductors to form a heterojunction is an effective method to enhance the photocatalytic property of $Bi_{12}O_{17}Cl_2$. On the other hand, silver iodide (AgI) is a photosensitive material used in the photography field. Recently, AgI has attracted wide attention due to its excellent photocatalytic property. But the micro-sized AgI is unstable and can be reduced to Ag^0 in light irradiation.[45,46] It has been found that a good substrate to disperse AgI could improve the stability and photoactivity of pure AgI, such as $AgI/Bi_2O_2CO_3$,[47] AgI/BiOI,[48] and AgI/CeO_2.[45] Furthermore, the corresponding conduction band of AgI is suitable for producing super oxygen species and enhancing the photooxidation ability. Therefore, the AgI/$Bi_{12}O_{17}Cl_2$ hybrid materials are expected to make up the shortcoming of the pure AgI and $Bi_{12}O_{17}Cl_2$. In addition, to the best of our knowledge, there has been no report about AgI/$Bi_{12}O_{17}Cl_2$ hybrid materials and their application in the environment treatment field.

In this work, AgI/$Bi_{12}O_{17}Cl_2$ hybrid photocatalysts were fabricated via a deposition−precipitation process. Different wt % (14%, 25%, 40%) of AgI were loaded on $Bi_{12}O_{17}Cl_2$, and the samples were denoted as x% AgI/$Bi_{12}O_{17}Cl_2$ (where x% = wt % of AgI from initial concentration of $Bi_{12}O_{17}Cl_2$). Sulfamethazine (SMZ), which belongs to the sulfonamide group of antibiotics, was chosen as the target pollutant. The morphology structures, optical properties, photoelectrical properties, and photocatalytic activities of photocatalysts were fully validated. Furthermore, the possible degradation mechanism by the AgI/$Bi_{12}O_{17}Cl_2$ composite was proposed. This work provides insight into the guideline of photocatalytic AgI/$Bi_{12}O_{17}Cl_2$ design and lays the groundwork for the application of AgI/$Bi_{12}O_{17}Cl_2$ as an efficient, stable, and low-cost visible light photocatalyst in wastewater treatment.

■ EXPERIMENTAL SECTION

Materials. The bismuth nitrate pentahydrate ($Bi(NO_3)_3·5H_2O$), ammonium chloride (NH_4Cl), ethylene glycol (EG), sodium hydroxide (NaOH), silver nitrate ($AgNO_3$), and potassium iodine (KI) were purchased from Sinopharm Chemical Reagent Corp, P. R. China. All chemicals were analytical grade and used as received without further purification. These aqueous solutions were prepared with ultrapure water (18.25 MΩ $cm^{−1}$) obtained from Millipore system.

Preparation of Catalysts. The $Bi_{12}O_{17}Cl_2$ was fabricated by a previously reported method with minor modifications.[49] In a typical procedure, 0.97 g (2 mmol) $Bi(NO_3)_3·5H_2O$ was dissolved in 10 mL EG. After 5 min stirring and 5 min sonication, the homogeneous solution was obtained. Then, 0.32 g (6 mmol) NH_4Cl and 0.80 g (20

mmol) NaOH were added to 60 mL distilled water under vigorous stirring for 10 min. The mixture was then poured into a 100 mL Teflon-lined stainless autoclave and heated at 140 °C for 12 h under the autogenous pressure. The resultant precipitate was collected and washed consecutively with deionized water and ethanol to remove residual ions. The final product was dried at 80 °C in air.

The AgI/$Bi_{12}O_{17}Cl_2$ heterojunction was fabricated by an in situ deposition−precipitation procedure. Typically, 0.70 g of $Bi_{12}O_{17}Cl_2$ was dispersed in 50 mL of deionized water under ultrasonic processing. Then, 0.17 g (1 mmol) $AgNO_3$ was added into the solution with the AgI amount in the composite set at 25%. After the solution was stirred in dark for 1 h, a stoichiometric amount of KI was slowly added into the suspension above. The suspension was stirred for another 1 h to synthesize the samples. The resulting precipitates were washed with deionized water and absolute ethanol several times and then dried at 70 °C. A series of AgI/$Bi_{12}O_{17}Cl_2$ composites with different mass ratios of AgI and $Bi_{12}O_{17}Cl_2$ were prepared by changing the amounts of AgI and marked as 14%, 25%, and 40%. As a reference, the pristine AgI was prepared without adding $Bi_{12}O_{17}Cl_2$ under the same conditions.

Characterization Methods. The crystal phase of the samples was determined by a D/max-2500 X-ray diffractometer (XRD; Rigaku, Japan) using Cu Kα radiation ($λ$ = 0.15406 nm) in the region of $2θ$ from 5° to 80°. X-ray photoelectron spectrum (XPS) of the samples was obtained by using an ESCALAB 250Xi spectrometer (Thermo Fisher, USA) with Al Kα radiation (hv = 1486.6 eV). The UV−vis diffuse reflectance spectra (DRS) were performed on a UV−vis spectrophotometer (Cary 300, USA) with an integrating sphere. The photoluminescence (PL) spectra were recorded with an Hitachi F-7000 fluorescence spectrophotometer at an excitation wavelength of 365 nm. Their morphology was examined by a transmission electron microscope (TEM, JEOL JEM-2100F). The total organic carbon (TOC) was applied to analyze the mineralization degree of organic contaminants on Analytik Jena AG (Multi N/C 2100). The electron spin resonance (ESR) signals of radicals spin-trapped by spin-trapping reagent 5,5-dimethyl-l-pyrroline-N-oxide (DMPO) and 2,2,6,6-tetra-methylpiperidinooxy (TEMPO) were examined on a Bruker ER200-SRC spectrometer under visible light irradiation ($λ$ > 420 nm).

Photocatalytic Experiments. In order to evaluate the photocatalytic activity of prepared samples, photocatalytic removal of SMZ was carried out under visible light irradiation using a 300 W Xe lamp (CELHXF300, China) with a 420 nm cut filter. Typically, the photocatalyst (50 mg) was suspended in 50 mL water containing SMZ (10 mg $L^{−1}$). Subsequently, the solution was magnetically stirred for 1 h in the dark to ensure the establishment of equilibrium between adsorption and desorption. After that, the mixture was exposed to visible light, and 1 mL of solution was taken out at given time interval, centrifuged, filtrated by 0.22 $μ$m membrane filter, and analyzed. The SMZ concentration was determined using an HPLC Series 1100 (Agilent, Waldbronn, Germany) equipped with a UV detector. The column was a C-18 column (4.6 mm × 250 mm) at a temperature of 30 °C. The mobile phase was water−acetonitrile (80:20, v/v) with 0.1% acetic acid at a flow rate 1 mL $min^{−1}$. The sample volumes for injection were all 20 $μ$L, and the wavelength of detector was 270 nm. A liquid chromatography mass spectrometry (LC−MS) (Agilent 1290/6460, Triple Quad MS, USA) was used to determine the intermediate products from SMZ degradation. The isocratic mobile phase was prepared by using 0.1% acetic acid and acetonitrile with the ratio of 70:30 (v/v), which was set at a flow rate of 0.1 mL $min^{−1}$. The gradient mobile phase was the combination of acetonitrile and 0.1% acetic acid. The gradient elution was programmed as follows: 0−1 min, 10% acetonitrile; 1−12 min, 10−90% acetonitrile; 12−15 min, 90% acetonitrile; 15−20 min, 10−90% acetonitrile.

Electrochemical Measurements. To prepare the electrodes, the catalyst was dispersed in a Nafion solution (0.5 wt %) to form a 10 mg $mL^{−1}$ solution. Here, 100 $μ$L of the resultant solution was then dip-coated on the pretreated fluorine-doped tin oxide (FTO) surface and allowed to dry in a vacuum oven for 24 h at room temperature. The photocurrent measurements were conducted on an electrochemical workstation (CHI660D Instruments) in a standard three-electrode

system with the catalyst-coated electrode as the working electrode, a Pt electrode (40 mm × 0.55 mm, 99%) as the counter electrode, and an Ag/AgCl electrode as the reference electrode. The 300 W xenon lamp with a 420 nm cutoff filter was utilized as the light source for the photocurrent (I-t) measurements. The electrochemical impedance spectroscopy (EIS) was also performed in a Na_2SO_4 aqueous solution with the above three-electrode system.

■ RESULTS AND DISCUSSION

**Catalysts Characterization.** The XRD patterns of investigated samples were shown in Figure 1. The patterns of
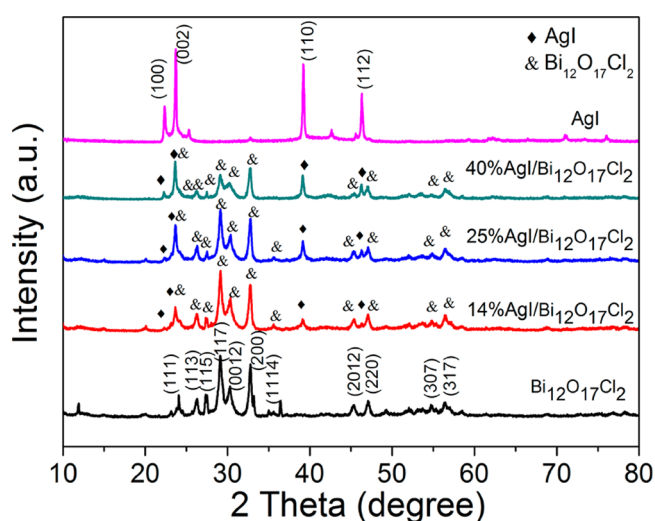
Figure 1. XRD patterns of samples AgI, $Bi_{12}O_{17}Cl_2$, and AgI/$Bi_{12}O_{17}Cl_2$ (14%, 25%, and 40%).

pristine $Bi_{12}O_{17}Cl_2$ and AgI agreed well with the standard phase of $Bi_{12}O_{17}Cl_2$ (JCPDS card no. 37-0702) and the standard cubic phase of AgI (JCPDS card no. 09-0374), respectively.[46,50] Characteristic peaks at 22.32°, 23.71°, 39.13°, and 46.31°, which, respectively, corresponded to lattice plane (100), (002), (110), and (112) of AgI, were all observed on AgI/$Bi_{12}O_{17}Cl_2$.

With the increase in the AgI amount, the diffraction peaks (115), (117), (200), and (220) of $Bi_{12}O_{17}Cl_2$ are also present in the pattern of AgI/$Bi_{12}O_{17}Cl_2$ and gradually get weaker. These results indicate that the growth of $Bi_{12}O_{17}Cl_2$ has been restrained by AgI in the formation of the crystals.[51]

The composition and chemical status of the as-prepared samples were also confirmed by XPS technique. As shown in Figure 2a, Ag 3d, I 3d, Bi 4f, O 1s, and Cl 2p were detected in the spectrum of 25% AgI/$Bi_{12}O_{17}Cl_2$. The doublet peaks of Ag $3d_{5/2}$ and Ag $3d_{3/2}$ could be divided into two individual peaks. The peak of Ag 3d was unsymmetrical, which indicated that there were two different valence states of silver in the catalysts. The peaks at 367.6 and 373.5 eV were attributed to Ag^+ in AgI, and those at 368.6 and 374.5 eV were assigned to Ag^0 species (Figure 2b).[52] The reason for the negative shift of Ag 3d XPS on going from 0 to +1 was that Ag^+ was partially reduced to Ag^0 during the synthesis process for AgI.[53] The peaks at 618.6 eV (I $3d_{5/2}$) and 630.9 eV (I $3d_{3/2}$) in the I 3d region are assigned to I^- in AgI (Figure 2c).[48] The binding energies of Bi $4f_{5/2}$ and Bi $4f_{7/2}$ are 164.2 and 158.9 eV for pristine $Bi_{12}O_{17}Cl_2$, respectively (Figure 2d). However, AgI/$Bi_{12}O_{17}Cl_2$ exhibits two distinct peaks of Bi $4f_{5/2}$ and Bi $4f_{7/2}$ separately locating at 164.9 and 159.3 eV, respectively. Compared with pristine $Bi_{12}O_{17}Cl_2$, a slight binding energy left-shift of Bi 4f peaks (164.2 shifts to 164.9 eV; 158.9 shifts to 159.3 eV) occurred over AgI/$Bi_{12}O_{17}Cl_2$, indicating that the chemical coordination environment of Bi^{3+} ions may be changed.[51,54] Figure 2e shows the Cl 2p peak of $Bi_{12}O_{17}Cl_2$. It exhibits two main peaks with binding energies at 199.1 and 197.3 eV, which can be ascribed to Cl $2p_{1/2}$ and Cl $2p_{3/2}$, respectively.[36] The O 1s fit well with the peak at 529.5 eV, which belongs to the bismuth oxygen bond in $Bi_{12}O_{17}Cl_2$ (Figure 2f). The obtained results were in good agreement with the XRD analysis.

The SEM images of morphology and EDS mapping of $Bi_{12}O_{17}Cl_2$, and AgI/$Bi_{12}O_{17}Cl_2$ are shown in Figure 3. The SEM images (Figure 3a) reveal that the sample possessed a nanolayer structure. The nanoparticles of AgI homogeneously disperse on the layer of $Bi_{12}O_{17}Cl_2$ (Figure 3b and c), which
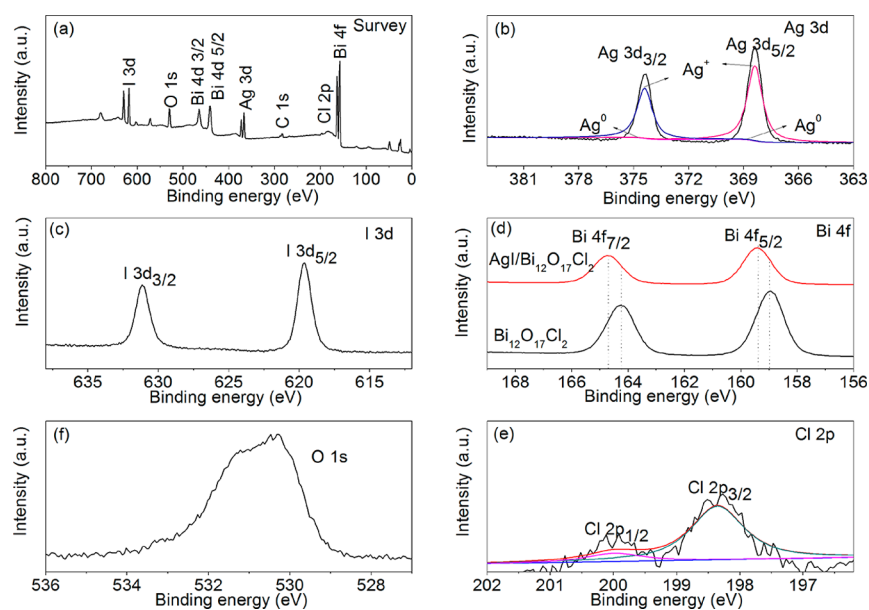

Figure 2. XPS spectra of 25% AgI/$Bi_{12}O_{17}Cl_2$ (a) survey spectra, (b) high resolution Ag 3d, (c) high resolution I 3d, (d) high resolution Bi 4f, (e) high resolution Cl 2p, and (f) high resolution O 1s.
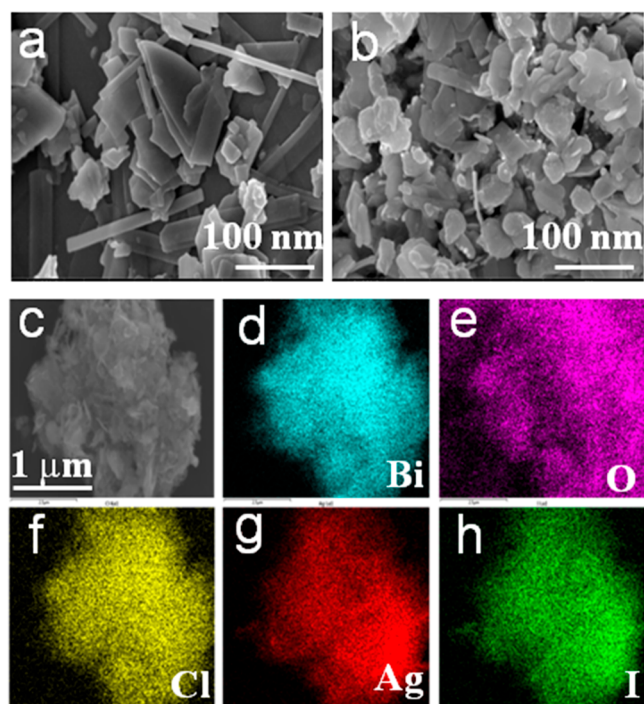
Figure 3. SEM images of (a) $Bi_{12}O_{17}Cl_2$, (b,c) 25% $AgI/Bi_{12}O_{17}Cl_2$, and (d−h) corresponding elemental maps of 25% $AgI/Bi_{12}O_{17}Cl_2$.

was further confirmed by TEM. The EDS data shown in Figure 3d−h confirm that the existence of Ag, I, Bi, O, and Cl were in the $AgI/Bi_{12}O_{17}Cl_2$.

The structures of AgI, $Bi_{12}O_{17}Cl_2$, and $AgI/Bi_{12}O_{17}Cl_2$ were further studied by TEM and HRTEM (Figure 4). It is shown in Figure 4a that pristine AgI is composed of large-scale nanoparticles with diameters ranging from 50 to 200 nm. As shown in Figure 4b, the as-prepared pristine $Bi_{12}O_{17}Cl_2$ sample reveals a clearly flat layer structure. The nanolayer has width and length ranges of 50−100 nm and 0.2−1.0 μm, respectively.
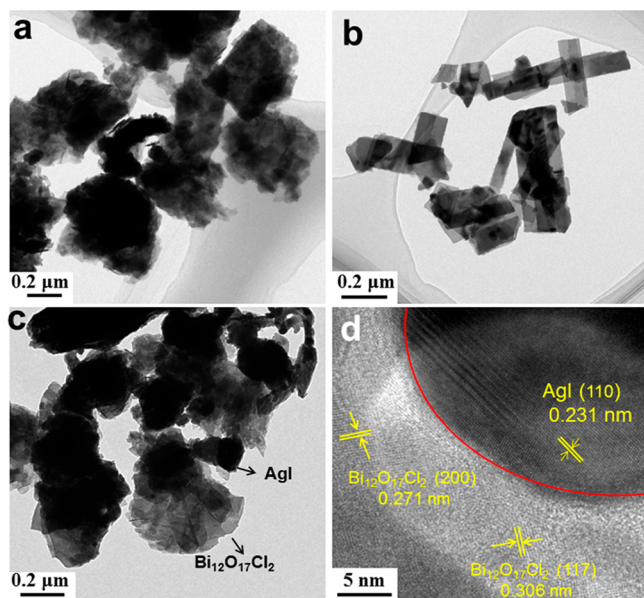
Figure 4. (a−c) TEM images of AgI, $Bi_{12}O_{17}Cl_2$ and 25% $AgI/Bi_{12}O_{17}Cl_2$, respectively. (d) High resolution TEM image of 25% $AgI/Bi_{12}O_{17}Cl_2$.

As shown in Figure 4c, a batch of nanoparticles developed from AgI are deposited on the surface of the $Bi_{12}O_{17}Cl_2$ nanosheets in $AgI/Bi_{12}O_{17}Cl_2$. In Figure 4d, the d-spacings of the lattice spacing of $Bi_{12}O_{17}Cl_2$ are 0.306 and 0.271 nm, corresponding to the (117) and (200) interlayer spacing, respectively, indicating there is no change in the lattice structure of $Bi_{12}O_{17}Cl_2$ after loading AgI.[42] Also, the d-spacing of AgI is 0.231 nm in $AgI/Bi_{12}O_{17}Cl_2$, corresponding to the (110) plane. HRTEM and SAED of single AgI and single $Bi_{12}O_{17}Cl_2$ are depicted in Figure S1. The results indicated that the heterojunction was constructed between AgI and $Bi_{12}O_{17}Cl_2$ in $AgI/Bi_{12}O_{17}Cl_2$ with interaction interfaces.

Optical Absorption Properties and Photoelectrical Properties. UV−vis diffuse reflectance spectroscopy (DRS) was conducted to evaluate the band gap energies (E_g) of the as-synthesized samples. As shown in Figure 5a, the absorption edges of pristine $Bi_{12}O_{17}Cl_2$ and AgI were located at about 520 and 475 nm, respectively. With increasing the mass ratio of AgI, the optical absorption edges were still located at between 475 and 520 nm, indicating that all the $AgI/Bi_{12}O_{17}Cl_2$ composites possessed visible light response. Compared with pristine $Bi_{12}O_{17}Cl_2$ and AgI, the optical absorption edges of 25% $AgI/Bi_{12}O_{17}Cl_2$ composites were red-shifted obviously. Their band gaps were calculated using eq 1:

$$\alpha h v = A(h v - E_g)^{n/2} \tag{1}$$

where α, h, v, E_g, and A are the absorption coefficient, Planck's constant, light frequency, band gap energy, and a constant, respectively; n is determined by the type of optical transition of a semiconductor (n = 1 for direct transition and n = 4 for indirect transition).[55] The optical transition of AgI was direct, and the band gap energy of AgI was measured at 2.78 eV (Figure 5b). However, $Bi_{12}O_{17}Cl_2$ is an indirect semiconductor. As shown in Figure 5b, $Bi_{12}O_{17}Cl_2$ was estimated from a plot of $(\alpha h v)^2$ as a function of the photon energy ($h v$) to be approximately 2.41 eV.

The photoluminescence (PL) spectra of the samples were studied and are shown in Figure S2. All samples exhibit an emission peak centered at about 680 nm. Compared with pristine $Bi_{12}O_{17}Cl_2$ and AgI, the $AgI/Bi_{12}O_{17}Cl_2$ composites show significant quenching of the PL. These results revealed that $AgI/Bi_{12}O_{17}Cl_2$ exhibited the best activity in terms of charge carrier density, hole−electron separation, and charge transportation than $Bi_{12}O_{17}Cl_2$ and AgI.

The I-t property has been verified to be an efficient approach to reflect the photogenerated charge separation in the heterojunction photocatalysts.[56,57] In Figure 6a, all samples presented good reproducibility of photocurrent under visible light. The photocurrent of $AgI/Bi_{12}O_{17}Cl_2$ was nearly 4 times higher than pristine $Bi_{12}O_{17}Cl_2$. The enhancement of photocurrent illustrated that the mobility of the charge carriers was promoted. This result suggested that the improved charge separations of carriers were realized in the heterojunction of $AgI/Bi_{12}O_{17}Cl_2$.

EIS is a versatile technique used to characterize phenomena such as corrosion, fuel cells, and batteries.[58,59] This technique could be used to explain the electron-transfer efficiency at the electrodes.[60] For further verifying the efficient separation of carriers, we measured the EIS of AgI, $Bi_{12}O_{17}Cl_2$, and $AgI/Bi_{12}O_{17}Cl_2$ (Figure 6b). $AgI/Bi_{12}O_{17}Cl_2$ displays the smallest arc radius in the EIS Nyquist plot compared to pristine AgI and $Bi_{12}O_{17}Cl_2$. It demonstrates that $AgI/Bi_{12}O_{17}Cl_2$ has low
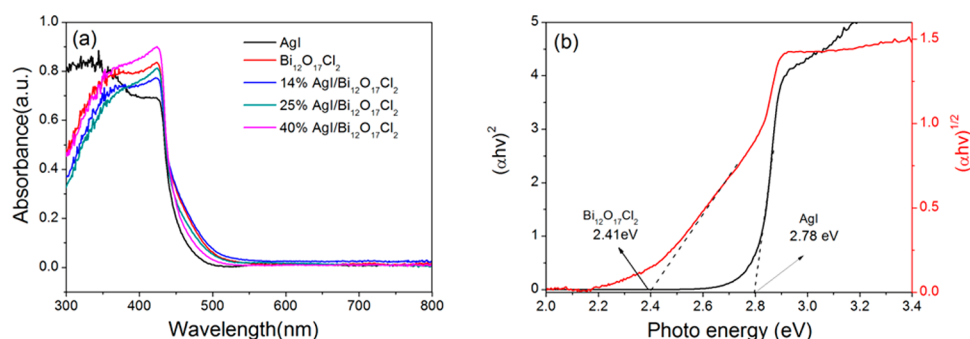
Figure 5. (a) UV−vis adsorption spectra of samples. (b) Plots of $(\alpha h\nu)^{1/2}$ vs photon energy $(h\nu)$ for $Bi_{12}O_{17}Cl_2$ and the plots of $(\alpha h\nu)^2$ vs photon energy $(h\nu)$ for AgI.
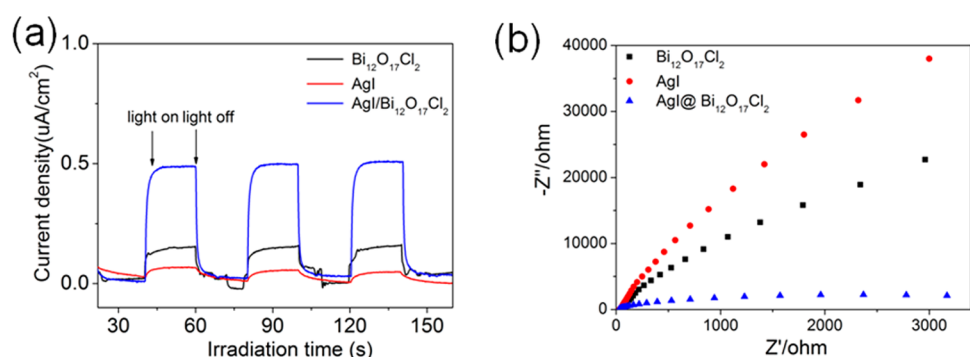
Figure 6. (a) Photocurrent transient measurement. (b) Electrochemical impedance spectra of photocatalysts.
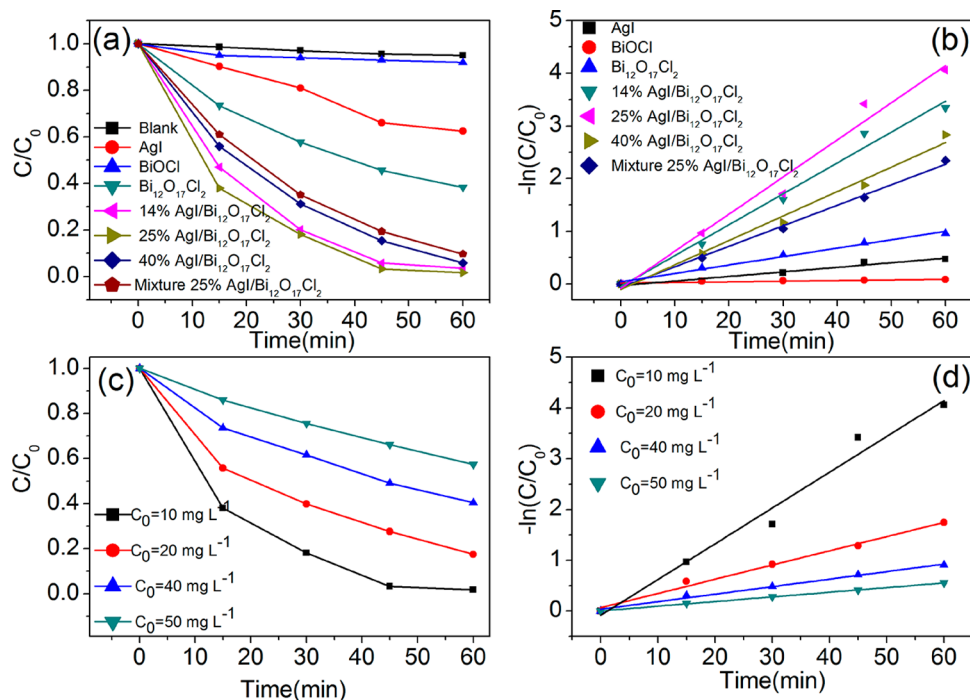
Figure 7. (a) Photodegradation rate of SMZ on different photocatalyst. (b) Kinetic fit of the degradation of SMZ on different photocatalyst samples. (c) Effect of initial concentration of SMZ on 25% $AgI/Bi_{12}O_{17}Cl_2$. (d) Kinetic fit of the initial concentration of SMZ on 25% $AgI/Bi_{12}O_{17}Cl_2$.

interfacial layer resistance, which agrees with the results of PL and I-t.

Photocatalytic Activity. The photocatalytic activities of the $AgI/Bi_{12}O_{17}Cl_2$ composites were measured by decomposing SMZ under visible light irradiation. SMZ is a kind of organic contaminant, which is difficult to decomposed.[61,62] Before

irradiation, a dark adsorption experiment was carried out to discuss the adsorption efficiency of the samples. As revealed in Table S1, there was no increasing adsorption after 30 min of dark adsorption. In our experiment, 60 min of dark adsorption was enough to reach the adsorption equilibrium between photocatalyst and SMZ. Figure 7a shows the photodegradation

of SMZ as a function of irradiation time over different photocatalysts. After irradiation for 60 min, the SMZ photodegradation did not occur in the absence of the photocatalyst, while pristine AgI and $Bi_{12}O_{17}Cl_2$ achieved the degradation efficiencies of 38.51% and 45.39%, respectively. All of the heterojunction samples (including 14%, 25%, 40% AgI/$Bi_{12}O_{17}Cl_2$) exhibited enhanced photocatalytic activities greatly. It suggested that AgI amounts played a crucial role in the photocatalytic activity, and a small amount of AgI (14%) over $Bi_{12}O_{17}Cl_2$ could lead to a sharp increase in SMZ decomposition from 45.39% to 83.26%. As the AgI amount increased to 25%, the highest photocatalytic activity was achieved, at which 96.15% of SMZ were decomposed. However, the photocatalytic activity decreased when the AgI amount rose to 40%. This result may be due to the excess of AgI facilitating the recombination of photoinduced carriers in the AgI/$Bi_{12}O_{17}Cl_2$ composite. According to the above results, the optimized amount of AgI in the AgI/$Bi_{12}O_{17}Cl_2$ composites was 25%. Besides, the photocatalytic performance of a mechanical mixture of 25% AgI/$Bi_{12}O_{17}Cl_2$ was also investigated. The degradation efficiency (83.15%) of the mechanical mixture is much lower than that obtained by using 25% AgI/$Bi_{12}O_{17}Cl_2$, suggesting that a heterojunction may be formed between AgI and $Bi_{12}O_{17}Cl_2$ through the intimate interfacial contact.

The degradation kinetics of SMZ was investigated by fitting the experimental data to the following pseudo-first-order kinetics equation:

$$-\ln(C_t/C_0) = kt \qquad (2)$$

where C_t is the instant of SMZ concentration, C_0 is the initial of SMZ concentration, and k (min^{-1}) is the apparent reaction rate constant. The entire sample could be fitted well by the pseudo-first-order kinetics model with a high fitting coefficient. In Figure 7b, the results showed that the highest k value for 25% AgI/$Bi_{12}O_{17}Cl_2$ was 0.070 min^{-1}, which was 7.8, 7.0, and 35 times higher than that of pristine $Bi_{12}O_{17}Cl_2$ (0.009 min^{-1}), AgI (0.010 min^{-1}), and BiOCl (0.002 min^{-1}), respectively.

Various initial concentrations of SMZ (10−50 mg L^{-1}) were used to test the activities of 25% AgI/$Bi_{12}O_{17}Cl_2$, and the results are depicted in Figure 7c. With increasing concentration, the removal efficiency decreased. The efficiency of 25% AgI/$Bi_{12}O_{17}Cl_2$ dropped from 96.15% (10 mg L^{-1}) to 43.26% (50 mg L^{-1}) in 1 h irradiation. As shown in Figure 7d, all samples could be fitted well by the pseudo-first-order kinetics model with high coefficients. This negative effect was explained by a certain amount of AgI/$Bi_{12}O_{17}Cl_2$ generating the same active species to remove SMZ. A lower concentration of initial pollutants can achieve a higher removal rate at the same time. Therefore, dilution was essential in the pretreatment of practical wastewater treatment.

The effective mineralization of organic compounds to avoid secondary pollution of photocatalytic technology is very important in practical applications. In this system, TOC was chosen as a mineralization index, and the time independence of the TOC data in the SMZ solution over 25% AgI/$Bi_{12}O_{17}Cl_2$ during the photocatalytic process is shown in Figure 8. As shown in Figure 8, the TOC of 25% AgI/$Bi_{12}O_{17}Cl_2$ was decreased with increasing illumination time. After 120 min irradiation, over 60% of TOC was eliminated, indicating that SMZ could be effectively mineralized by the as-prepared 25% AgI/$Bi_{12}O_{17}Cl_2$ under visible light irradiation. Furthermore, the TOC of pristine $Bi_{12}O_{17}Cl_2$ was also studied (Figure S4).
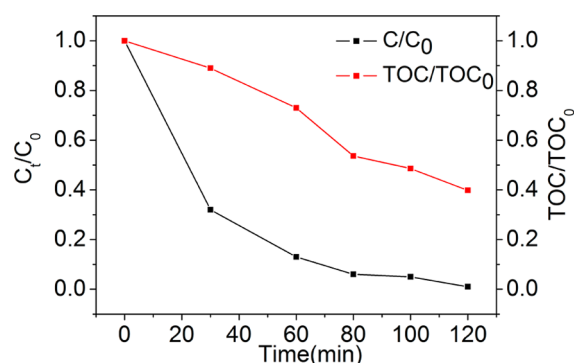

Figure 8. TOC degraded efficiencies of SMZ on 25% AgI/$Bi_{12}O_{17}Cl_2$.

From the viewpoint of practical applications, $Bi_{12}O_{17}Cl_2$ and the 25% AgI/$Bi_{12}O_{17}Cl_2$ composite were selected to evaluate the reusability of the as-prepared composites. As shown in Figure 9, AgI/$Bi_{12}O_{17}Cl_2$ showed a good catalytic stability and
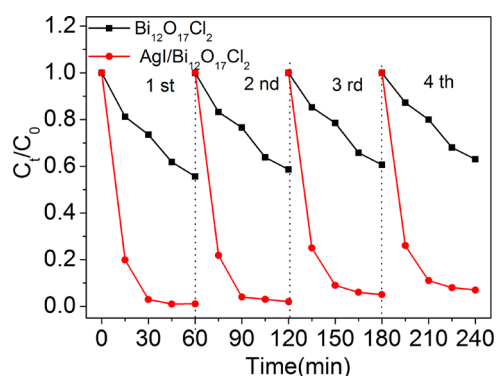

Figure 9. Cycle runs in photodegradation of SMZ over 25% AgI/$Bi_{12}O_{17}Cl_2$.

maintained a similar reactivity after four cycles. Compared to AgI/$Bi_{12}O_{17}Cl_2$, the degradation efficiency of $Bi_{12}O_{17}Cl_2$ exists as a significant loss. The composition of the recycled AgI/$Bi_{12}O_{17}Cl_2$ composite was also characterized by XRD. As shown in Figure S3, the XRD patterns of the AgI/$Bi_{12}O_{17}Cl_2$ sample after the photocatalytic reactions reveal that its crystal structure remained unchanged. Therefore, AgI/$Bi_{12}O_{17}Cl_2$ is a stable and efficient photocatalyst for degradation of organic pollutants, which is helpful for practical applications in the future.

To understand the photodegradation mechanism of SMZ, the free radicals, holes (h^+), superoxide radical anions ($\bullet O_2^-$), and hydroxyl radicals ($\bullet OH$) trapping experiments were carried out to identify the main active species taking part in the degradation process. According to the previous report, different scavengers (ethylenediaminetetraacetic acid disodium salt as a hole scavenger, isopropyl alcohol as an $\bullet OH$ scavenger, and benzoquinone as an $\bullet O_2^-$ scavenger) could be used to trap the free radicals.[63−65] As shown in Figure 10a, the photo-degradation rates of pristine $Bi_{12}O_{17}Cl_2$ were obviously suppressed with the presence of benzoquinone (BQ) or ethylenediaminetetraacetic acid disodium (EDTA-2Na). The removal efficiency of SMZ decreased from 52.23% to 18.12% with the addition of 1 mM EDTA-2Na. The addition of 1 mM isopropyl alcohol (IPA) had slightly suppressed the decomposition of SMZ, implying that $\bullet OH$ played an insignificant role in the decomposition of SMZ under visible light irradiation. It demonstrated that the photogenerated holes
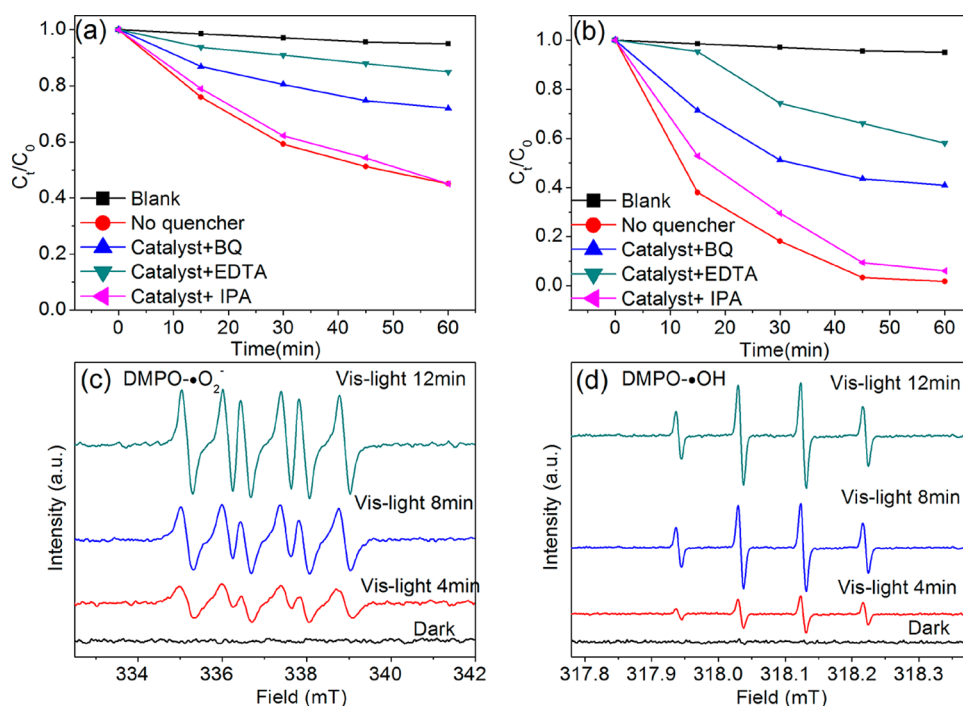
Figure 10. Photocatalytic degradation plots of SMZ over (a) $Bi_{12}O_{17}Cl_2$ and (b) 25% $AgI/Bi_{12}O_{17}Cl_2$ with the addition of hole, $\bullet O_2^-$, and $\bullet OH$ radical scavenger under visible light irradiation. ESR spectra of 25% $AgI/Bi_{12}O_{17}Cl_2$ dispersion under both dark and visible light irradiation (>420 nm) condition: (c) in methanol dispersion for DMPO-$\bullet O_2^-$ and (d) in aqueous dispersion for DMPO-$\bullet OH$.

and $\bullet O_2^-$ were the predominant oxidant in the photocatalytic degradation of SMZ for pristine $Bi_{12}O_{17}Cl_2$. As shown in Figure 10b, the photocatalytic activity of $AgI/Bi_{12}O_{17}Cl_2$ was greatly suppressed by the addition of these three scavengers. The inhibition efficiencies for the removal of SMZ were estimated to be 30.53% for EDTA-2Na and 25.89% for BQ. Thus, it could be deduced that holes, $\bullet O_2^-$, and $\bullet OH$ were in $AgI/Bi_{12}O_{17}Cl_2$.

Moreover, in order to further confirm the main active species in this catalytic system under visible irradiation, the ESR spin-trap with the DMPO technique was performed on the illuminated $AgI/Bi_{12}O_{17}Cl_2$ composite (Figure 10c and d).[66] As shown in Figure 10c, four obvious signals with $AgI/Bi_{12}O_{17}Cl_2$ in methanol were produced, which could be assigned to DMPO-$\bullet O_2^-$ under light illumination. There is no $\bullet O_2^{-2}$ signal in the dark, but an increasing signal of DMPO-$\bullet O_2^{-2}$ could be observed with visible light irradiation. Moreover, the signal of $\bullet OH$ was also detected in the DMPO system when exposed to light in Figure 10d. The results of ESR were well consistent with the trapping experiment. It revealed that the degradation mechanism of the $AgI/Bi_{12}O_{17}Cl_2$ composite has been changed compared with that of pristine $Bi_{12}O_{17}Cl_2$.

Degradation Pathway of SMZ by $AgI/Bi_{12}O_{17}Cl_2$. The removal efficiency of $AgI/Bi_{12}O_{17}Cl_2$ was also shown in Figure S5. The SMZ (t = 3.89 min) concentration gradually decreased with the increase in irradiation time and became undetectable after 120 min irradiation. It indicated that most of the pollutants were mineralized to small inorganic molecules, like CO_2 and H_2O under the photocatalytic degradation process after 120 min irradiation, further revealing the strong photo-oxidation capability of the $AgI/Bi_{12}O_{17}Cl_2$ heterojunction.

To further understand the degradation mechanism of SMZ (denoted as P1) in the $AgI/Bi_{12}O_{17}Cl_2$ system under visible irradiation, HPLC-MS was used to identify the degradation intermediates. As shown in Figure S6, SMZ and other four

main degradation products were observed. The molecular weight for P1 is 278.33. Since the electrospray ionization (ESI) source was used in HPLC-MS, the m/z was M+H$^+$. With the prolongation of irradiation time, the concentration of P1 (m/z value of 279.3) decreased gradually. Meanwhile, the four intermediates including P2 (m/z value of 309.0), P3 (m/z value of 339.3), P4 (m/z value of 215.1), and P5 (m/z value of 124.0) were formed in 30 min irradiation. After 120 min irradiation, the intermediate P2 disappeared, and the concentration of intermediates including P3, P4, and P5 were decreased. As shown in Figure 11, three degradation pathways have been proposed: (1) The initial product of SMZ was P2 (m/z value of 309.0), which was formed through the oxidation of amidogen on the benzene ring. Subsequently, the P3 (m/z value of 339.3) was produced by further oxidation via
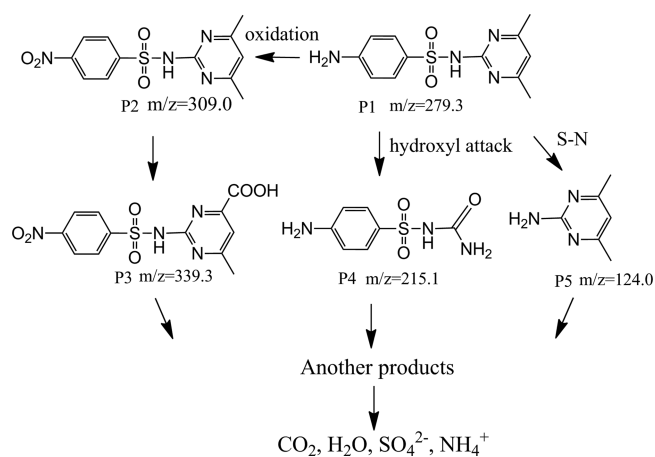
Figure 11. Proposed SMZ photodegradation pathway by the 25% $AgI/Bi_{12}O_{17}Cl_2$ photocatalyst.

carboxylation of the methyl group. (2) The P4 (*m/z* value of 215.1) was produced by the decay of the pyrimidine ring forming urea in SMZ. (3) The P5 (*m/z* value of 124.0) was produced by the hydroxyl radicals attack on the SMZ which resulted in cleavage of the S−N bond on SMZ and further formed the pyrimidine ring. The proposed reaction route has a correlation with the kinetic results. The concentration of SMZ was decreased rapidly in the first 60 min irradiation (Figure 8). At this time, the TOC removal rate was increased slowly due to the large molecular weight intermediates (like P2 and P3) generated. With the extension of irradiation time, the concentration of SMZ was in a low level, and the intermediates (like P4 and P5) began to decompose, then the TOC removal rate was increased rapidly. The degradation products did not accumulate during the photocatalytic system, and their concentrations were at a low level. These degradation products would decompose into small molecules, such as H_2O, CO_2, and NH_4^+.

Possible Degradation Mechanism. The high photocatalytic activity of the as-synthesized $AgI/Bi_{12}O_{17}Cl_2$ composites may be related to their unique band. Different conduction band (CB) and valence band (VB) levels can change the efficiency of charge transfer.[67] The Mott-Schottky plots of pristine AgI and $Bi_{12}O_{17}Cl_2$ are shown in Figure S7a. The flat potentials of pristine AgI and $Bi_{12}O_{17}Cl_2$ were calculated to be −0.42 and −0.48 V versus the $Hg/HgCl_2$ electrode (SCE), respectively. They were equivalent to −0.18 and −0.24 V versus the normal hydrogen electrode (NHE), respectively. The flat potential is almost equal to that of the Fermi level.[68] Besides, Figure S7b shows the VB-XPS spectra of pristine AgI and $Bi_{12}O_{17}Cl_2$. It shows that the gap between the Fermi level and VB was 1.49 eV for AgI, while it was 1.74 eV for $Bi_{12}O_{17}Cl_2$. So, the VB values of pristine AgI and $Bi_{12}O_{17}Cl_2$ were equal to 1.31 and 1.50 eV, respectively. According to the previous result, the band gap energys of AgI and $Bi_{12}O_{17}Cl_2$ were measured at 2.78 and 2.41 eV, respectively. So, the CB values of AgI and $Bi_{12}O_{17}Cl_2$ were found to be −1.47 and −0.91 eV, respectively. After AgI and $Bi_{12}O_{17}Cl_2$ contact, the higher Fermi energy of $Bi_{12}O_{17}Cl_2$ than AgI caused the energy bands of $Bi_{12}O_{17}Cl_2$ to bend upward and AgI to bend downward toward the interface to reach electrical equilibrium. Therefore, the possible mechanism was proposed based on the above results.[47] As shown in Figure 12, under visible light irradiation, both AgI and
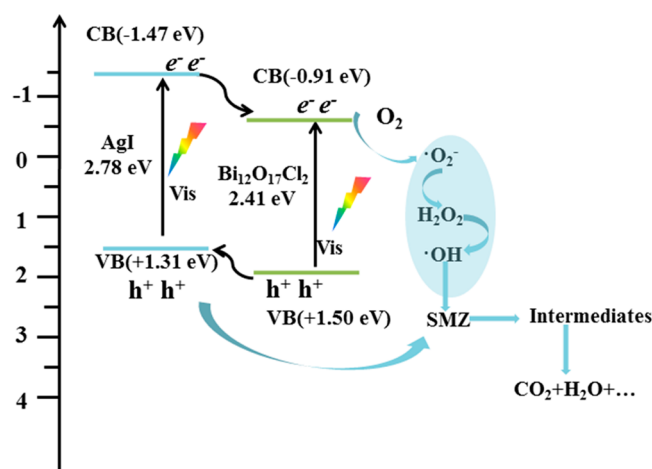
$Bi_{12}O_{17}Cl_2$ could excite hole and electron, and the electrons of the CB of AgI would transfer to the CB of $Bi_{12}O_{17}Cl_2$ to reduce surface O_2 into the oxidize species $\bullet O_2^-$. Then, parts of $\bullet O_2^-$ reacted with H^+ and generated H_2O_2, which was further excited by electrons and changed into $\bullet OH$. The holes of $Bi_{12}O_{17}Cl_2$ would be transferred to VB of AgI, and the holes of VB of AgI could directly oxidize organic pollutants into a small molecular. In this route, the electrons and holes could be separated efficiently, leading to the high photocatalytic activity of $AgI/Bi_{12}O_{17}Cl_2$. The active species, holes, $\bullet O_2^-$, and $\bullet OH$ could further effectively degrade the target pollutant (SMZ) into more small intermediates or directly into end products (CO_2 and H_2O). Furthermore, the photogenerated electrons of AgI tend to be migrating to $Bi_{12}O_{17}Cl_2$, which may avoid AgI reduced to Ag and further enhance the stability of AgI under visible irradiation.

CONCLUSIONS

In summary, a visible-light-driven catalyst system has been developed using AgI and hydrothermal prepared $Bi_{12}O_{17}Cl_2$ as a photocatalyst to make contact heterostructure for efficient degradation of SMZ. The characterizations showed AgI nanoparticles evenly distributed on the surface of $Bi_{12}O_{17}Cl_2$, and heterostructures were formed. The degradation rate of SMZ by $AgI/Bi_{12}O_{17}Cl_2$ was about 7.8 times and 35.2 times higher than that of pristine $Bi_{12}O_{17}Cl_2$ and BiOCl under visible-light-driven photocatalysts, respectively. It was also found that the AgI amount in the $AgI/Bi_{12}O_{17}Cl_2$ composites played an important role in the corresponding photocatalytic properties, and the optimized ratio was obtained at 25%. The dramatic enhancement in the visible light photocatalytic activity can be attributed to the effective photogenerated charge transfer at the interface of AgI and $Bi_{12}O_{17}Cl_2$. High photocurrent intensity, great mineralization ability, and excellent photostability were also obtained for the $AgI/Bi_{12}O_{17}Cl_2$ sample. The SMZ degradation pathway can be divided into three steps: cleaving, aromatic ring opening, and mineralizing. The photogenerated reactive species and degradation intermediates are identified, and a photocatalytic mechanism is proposed. Moreover, these composites could apply to other contaminant degradation in wastewater and treated effluent water.

ASSOCIATED CONTENT

ⓢ Supporting Information

The Supporting Information is available free of charge on the ACS Publications website at DOI: 10.1021/acssuschemeng.7b04584.

TEM images, photoluminescence, Mott-Schottky plots, XPS-VB of the prepared samples, photocatalytic degradation, TOC removal, and HPLC-MS analysis of SMZ by the prepared samples. (PDF)

AUTHOR INFORMATION

Corresponding Authors
*E-mail: zgming@hnu.edu.cn (G.M. Zeng). Tel.: +86−731−88822754.
*E-mail: huangdanlian@hnu.edu.cn (D.L. Huang). Tel.: +86−731−88823701.

ORCID ⓘ
Guangming Zeng: 0000-0002-4230-7647
Danlian Huang: 0000-0003-4955-5755

Figure 12. Schematic of mechanism of photocatalytic SMZ degradation on 25% $AgI/Bi_{12}O_{17}Cl_2$.

■ **REFERENCES**

(1) Watkinson, A. J.; Murby, E. J.; Costanzo, S. D. Removal of antibiotics in conventional and advanced wastewater treatment: Implications for environmental discharge and wastewater recycling. *Water Res.* **2007**, *41* (18), 4164−4176.

(2) Watkinson, A. J.; Murby, E. J.; Kolpin, D. W.; Costanzo, S. D. The occurrence of antibiotics in an urban watershed: From wastewater to drinking water. *Sci. Total Environ.* **2009**, *407* (8), 2711−2723.

(3) Huang, D.-L.; Wang, R.-Z.; Liu, Y.-G.; Zeng, G.-M.; Lai, C.; Xu, P.; Lu, B.-A.; Xu, J.-J.; Wang, C.; Huang, C. Application of molecularly imprinted polymers in wastewater treatment: a review. *Environ. Sci. Pollut. Res.* **2015**, *22* (2), 963−977.

(4) Huang, D.; Xue, W.; Zeng, G.; Wan, J.; Chen, G.; Huang, C.; Zhang, C.; Cheng, M.; Xu, P. Immobilization of Cd in river sediments by sodium alginate modified nanoscale zero-valent iron: Impact on enzyme activities and microbial community diversity. *Water Res.* **2016**, *106*, 15−25.

(5) Zeng, G.; Wan, J.; Huang, D.; Hu, L.; Huang, C.; Cheng, M.; Xue, W.; Gong, X.; Wang, R.; Jiang, D. Precipitation, adsorption and rhizosphere effect: The mechanisms for Phosphate-induced Pb immobilization in soils—A review. *J. Hazard. Mater.* **2017**, *339*, 354−367.

(6) Hu, L.; Wan, J.; Zeng, G.; Chen, A.; Chen, G.; Huang, Z.; He, K.; Cheng, M.; Zhou, C.; Xiong, W.; Lai, C.; Xu, P. Comprehensive evaluation of the cytotoxicity of CdSe/ZnS quantum dots in Phanerochaete chrysosporium by cellular uptake and oxidative stress. *Environ. Sci.: Nano* **2017**, *4* (10), 2018−2029.

(7) Zhang, Y.; Zeng, G.-M.; Tang, L.; Huang, D.-L.; Jiang, X.-Y.; Chen, Y.-N. A hydroquinone biosensor using modified core−shell magnetic nanoparticles supported on carbon paste electrode. *Biosens. Bioelectron.* **2007**, *22* (9−10), 2121−2126.

(8) Cheng, Y.; He, H.; Yang, C.; Zeng, G.; Li, X.; Chen, H.; Yu, G. Challenges and solutions for biofiltration of hydrophobic volatile organic compounds. *Biotechnol. Adv.* **2016**, *34* (6), 1091−1102.

(9) Huang, D.; Liu, L.; Zeng, G.; Xu, P.; Huang, C.; Deng, L.; Wang, R.; Wan, J. The effects of rice straw biochar on indigenous microbial community and enzymes activity in heavy metal-contaminated sediment. *Chemosphere* **2017**, *174*, 545−553.

(10) Grandclement, C.; Seyssiecq, I.; Piram, A.; Wong-Wah-Chung, P.; Vanot, G.; Tiliacos, N.; Roche, N.; Doumenq, P. From the conventional biological wastewater treatment to hybrid processes, the evaluation of organic micropollutant removal: a review. *Water Res.* **2017**, *111*, 297.

(11) Gong, J.-L.; Wang, B.; Zeng, G.-M.; Yang, C.-P.; Niu, C.-G.; Niu, Q.-Y.; Zhou, W.-J.; Liang, Y. Removal of cationic dyes from aqueous solution using magnetic multi-wall carbon nanotube nanocomposite as adsorbent. *J. Hazard. Mater.* **2009**, *164* (2−3), 1517−1522.

(12) Xu, P.; Zeng, G. M.; Huang, D. L.; Feng, C. L.; Hu, S.; Zhao, M. H.; Lai, C.; Wei, Z.; Huang, C.; Xie, G. X.; Liu, Z. F. Use of iron oxide nanomaterials in wastewater treatment: A review. *Sci. Total Environ.* **2012**, *424*, 1−10.

(13) Feng, Y.; Gong, J.-L.; Zeng, G.-M.; Niu, Q.-Y.; Zhang, H.-Y.; Niu, C.-G.; Deng, J.-H.; Yan, M. Adsorption of Cd (II) and Zn (II) from aqueous solutions using magnetic hydroxyapatite nanoparticles as adsorbents. *Chem. Eng. J.* **2010**, *162* (2), 487−494.

(14) Zhang, C.; Lai, C.; Zeng, G.; Huang, D.; Yang, C.; Wang, Y.; Zhou, Y.; Cheng, M. Efficacy of carbonaceous nanocomposites for sorbing ionizable antibiotic sulfamethazine from aqueous solution. *Water Res.* **2016**, *95*, 103−112.

(15) Zhong, S.; Zhou, C.; Zhang, X.; Zhou, H.; Li, H.; Zhu, X.; Wang, Y. A novel molecularly imprinted material based on magnetic halloysite nanotubes for rapid enrichment of 2, 4-dichlorophenoxyacetic acid in water. *J. Hazard. Mater.* **2014**, *276*, 58−65.

(16) Zhou, C.; Li, H.; Zhou, H.; Wang, H.; Yang, P.; Zhong, S. Water-compatible halloysite-imprinted polymer by Pickering emulsion polymerization for the selective recognition of herbicides. *J. sep. sci.* **2015**, *38* (8), 1365−1371.

(17) Hu, X.-j.; Wang, J.-s.; Liu, Y.-g.; Li, X.; Zeng, G.-m.; Bao, Z.-l.; Zeng, X.-x.; Chen, A.-w.; Long, F. Adsorption of chromium (VI) by ethylenediamine-modified cross-linked magnetic chitosan resin: Isotherms, kinetics and thermodynamics. *J. Hazard. Mater.* **2011**, *185* (1), 306−314.

(18) Huang, D.; Hu, C.; Zeng, G.; Cheng, M.; Xu, P.; Gong, X.; Wang, R.; Xue, W. Combination of Fenton processes and biotreatment for wastewater treatment and soil remediation. *Sci. Total Environ.* **2017**, *574*, 1599−1610.

(19) Cheng, M.; Zeng, G.; Huang, D.; Lai, C.; Xu, P.; Zhang, C.; Liu, Y. Hydroxyl radicals based advanced oxidation processes (AOPs) for remediation of soils contaminated with organic compounds: A review. *Chem. Eng. J.* **2016**, *284*, 582−598.

(20) Cheng, M.; Zeng, G.; Huang, D.; Lai, C.; Xu, P.; Zhang, C.; Liu, Y.; Wan, J.; Gong, X.; Zhu, Y. Degradation of atrazine by a novel Fenton-like process and assessment the influence on the treated soil. *J. Hazard. Mater.* **2016**, *312*, 184−191.

(21) Huang, D.-L.; Zeng, G.-M.; Feng, C.-L.; Hu, S.; Jiang, X.-Y.; Tang, L.; Su, F.-F.; Zhang, Y.; Zeng, W.; Liu, H.-L. Degradation of lead-contaminated lignocellulosic waste by Phanerochaete chrysosporium and the reduction of lead toxicity. *Environ. Sci. Technol.* **2008**, *42* (13), 4946−4951.

(22) Gao, Y.-q.; Gao, N.-y.; Deng, Y.; Yang, Y.-q.; Ma, Y. Ultraviolet (UV) light-activated persulfate oxidation of sulfamethazine in water. *Chem. Eng. J.* **2012**, *195−196*, 248−253.

(23) Yang, C.; Chen, H.; Zeng, G.; Yu, G.; Luo, S. Biomass accumulation and control strategies in gas biofiltration. *Biotechnol. Adv.* **2010**, *28* (4), 531−540.

(24) Polesel, F.; Andersen, H. R.; Trapp, S.; Plósz, B. G. Removal of Antibiotics in Biological Wastewater Treatment Systems A Critical Assessment Using the Activated Sludge Modeling Framework for Xenobiotics (ASM-X). *Environ. Sci. Technol.* **2016**, *50* (19), 10316−10334.

(25) Lu, Z.; Zeng, L.; Song, W.; Qin, Z.; Zeng, D.; Xie, C. In situ synthesis of C-TiO$_2$/g-C$_3$N$_4$ heterojunction nanocomposite as highly visible light active photocatalyst originated from effective interfacial charge transfer. *Appl. Catal., B* **2017**, *202*, 489−499.

(26) Lai, C.; Wang, M.-M.; Zeng, G.-M.; Liu, Y.-G.; Huang, D.-L.; Zhang, C.; Wang, R.-Z.; Xu, P.; Cheng, M.; Huang, C.; et al. Synthesis of surface molecular imprinted TiO$_2$/graphene photocatalyst and its highly efficient photocatalytic degradation of target pollutant under visible light irradiation. *Appl. Surf. Sci.* **2016**, *390*, 368−376.

(27) Chen, F.; Yang, Q.; Wang, Y.; Zhao, J.; Wang, D.; Li, X.; Guo, Z.; Wang, H.; Deng, Y.; Niu, C.; Zeng, G. Novel ternary heterojunction photococatalyst of Ag nanoparticles and g-C3N4 nanosheets co-modified BiVO$_4$ for wider spectrum visible-light photocatalytic degradation of refractory pollutant. *Appl. Catal., B* **2017**, *205*, 133−147.

(28) Zhou, C. Y.; Lai, C.; Huang, D. L.; Zeng, G. M.; Zhang, C.; Cheng, M.; Hu, L.; Wan, J.; Xiong, W. P.; Wen, M.; Wen, X. F.; Qin, L. Highly porous carbon nitride by supramolecular preassembly of monomers for photocatalytic removal of sulfamethazine under visible light driven. *Appl. Catal., B* **2018**, *220*, 202−210.

(29) Li, K.; Han, M.; Chen, R.; Li, S.-L.; Xie, S.-L.; Mao, C.; Bu, X.; Cao, X.-L.; Dong, L.-Z.; Feng, P.; Lan, Y.-Q. Hexagonal@Cubic CdS Core@Shell Nanorod Photocatalyst for Highly Active Production of H2 with Unprecedented Stability. *Adv. Mater.* **2016**, *28* (40), 8906−8911.

(30) Yang, S.-F.; Niu, C.-G.; Huang, D.; Zhang, H.; Liang, C.; Zeng, G. SrTiO3 nanocubes decorated with Ag/AgCl nanoparticles as photocatalysts with enhanced visible-light photocatalytic activity towards the degradation of dyes, phenol and bisphenol A. *Environ. Sci.: Nano* **2017**, *4* (3), 585−595.

(31) Wang, C.-Y.; Zhang, X.; Song, X.-N.; Wang, W.-K.; Yu, H.-Q. Novel Bi12O15Cl6Photocatalyst for the Degradation of Bisphenol A under Visible-Light Irradiation. *ACS Appl. Mater. Interfaces* **2016**, *8* (8), 5320−5326.

(32) Li, H.; Zhang, L. Photocatalytic performance of different exposed crystal facets of BiOCl. *Opin. Green Sus. Chem.* **2017**, *6*, 48.

(33) Li, J.; Li, H.; Zhan, G.; Zhang, L. Solar Water Splitting and Nitrogen Fixation with Layered Bismuth Oxyhalides. *Acc. Chem. Res.* **2017**, *50* (1), 112−121.

(34) Tang, L.; Zeng, G.-M.; Shen, G.-L.; Li, Y.-P.; Zhang, Y.; Huang, D.-L. Rapid detection of picloram in agricultural field samples using a disposable immunomembrane-based electrochemical sensor. *Environ. Sci. Technol.* **2008**, *42* (4), 1207−1212.

(35) Liu, J.; Zhao, H.; Wu, M.; Van der Schueren, B.; Li, Y.; Deparis, O.; Ye, J.; Ozin, G. A.; Hasan, T.; Su, B.-L. Slow Photons for Photocatalysis and Photovoltaics. *Adv. Mater.* **2017**, *29* (17), 1605349.

(36) Li, H.; Qin, F.; Yang, Z.; Cui, X.; Wang, J.; Zhang, L. New Reaction Pathway Induced by Plasmon for Selective Benzyl Alcohol Oxidation on BiOCl Possessing Oxygen Vacancies. *J. Am. Chem. Soc.* **2017**, *139* (9), 3513−3521.

(37) Li, J.; Zhao, K.; Yu, Y.; Zhang, L. Facet-Level Mechanistic Insights into General Homogeneous Carbon Doping for Enhanced Solar-to-Hydrogen Conversion. *Adv. Funct. Mater.* **2015**, *25* (14), 2189−2201.

(38) Wang, L.; Shang, J.; Hao, W.; Jiang, S.; Huang, S.; Wang, T.; Sun, Z.; Du, Y.; Dou, S.; Xie, T.; et al. A dye-sensitized visible light photocatalyst-Bi24O31Cl10. *Sci. Rep.* **2015**, *4*, 7384.

(39) Meng, X.; Zhang, G.; Li, N. Bi2Ga2O39 for visible light photocatalytic reduction of Cr(VI): Controlled synthesis, facet-dependent activity and DFT study. *Chem. Eng. J.* **2017**, *314*, 249−256.

(40) Li, J.; Wu, X.; Pan, W.; Zhang, G.; Chen, H. Vacancy-Rich Monolayer BiO2−x as a Highly Efficient UV, Visible, and Near-Infrared Responsive Photocatalyst. *Angew. Chem.* **2018**, *130*, 500−504.

(41) Wang, C.-Y.; Zhang, X.; Qiu, H.-B.; Wang, W.-K.; Huang, G.-X.; Jiang, J.; Yu, H.-Q. Photocatalytic degradation of bisphenol A by oxygen-rich and highly visible-light responsive Bi12O17Cl2 nanobelts. *Appl. Catal., B* **2017**, *200*, 659−665.

(42) Li, H.; Zhang, L. Oxygen vacancy induced selective silver deposition on the {001} facets of BiOCl single-crystalline nanosheets for enhanced Cr(vi) and sodium pentachlorophenate removal under visible light. *Nanoscale* **2014**, *6* (14), 7805.

(43) Li, J.; Zhan, G.; Yu, Y.; Zhang, L. Superior visible light hydrogen evolution of Janus bilayer junctions via atomic-level charge flow steering. *Nat. Commun.* **2016**, *7*, 11480.

(44) Xiao, X.; Jiang, J.; Zhang, L. Selective oxidation of benzyl alcohol into benzaldehyde over semiconductors under visible light: The case of Bi12O17Cl2 nanobelts. *Appl. Catal., B* **2013**, *142-143*, 487−493.

(45) Wen, X.-J.; Niu, C.-G.; Ruan, M.; Zhang, L.; Zeng, G.-M. AgI nanoparticles-decorated CeO2 microsheets photocatalyst for the degradation of organic dye and tetracycline under visible-light irradiation. *J. Colloid Interface Sci.* **2017**, *497*, 368−377.

(46) Wan, Z.; Zhang, G. Synthesis and facet-dependent enhanced photocatalytic activity of Bi2SiO5/AgI nanoplate photocatalysts. *J. Mater. Chem. A* **2015**, *3* (32), 16737−16745.

(47) Zhang, L.; Hu, C.; Ji, H. p-AgI anchored on {001} facets of n-Bi2O2CO3 sheets with enhanced photocatalytic activity and stability. *Appl. Catal., B* **2017**, *205*, 34−41.

(48) Ning, S.; Lin, H.; Tong, Y.; Zhang, X.; Lin, Q.; Zhang, Y.; Long, J.; Wang, X. Dual couples Bi metal depositing and Ag@AgI islanding on BiOI 3D architectures for synergistic bactericidal mechanism of E. coli under visible light. *Appl. Catal., B* **2017**, *204*, 1−10.

(49) Wang, C.-Y.; Zhang, X.; Qiu, H.-B.; Huang, G.-X.; Yu, H.-Q. Bi24O31Br10 nanosheets with controllable thickness for visible−light−driven catalytic degradation of tetracycline hydrochloride. *Appl. Catal., B* **2017**, *205*, 615−623.

(50) He, G.; Xing, C.; Xiao, X.; Hu, R.; Zuo, X.; Nan, J. Facile synthesis of flower-like Bi12O17Cl2/β-Bi2O3 composites with enhanced visible light photocatalytic performance for the degradation of 4-tert-butylphenol. *Appl. Catal., B* **2015**, *170−171*, 1−9.

(51) Huang, H.; Xiao, K.; He, Y.; Zhang, T.; Dong, F.; Du, X.; Zhang, Y. In situ assembly of BiOI@Bi12O17Cl2 p−n junction: charge induced unique front-lateral surfaces coupling heterostructure with high exposure of BiOI {001} active facets for robust and nonselective photocatalysis. *Appl. Catal., B* **2016**, *199*, 75−86.

(52) Wang, T.; Quan, W.; Jiang, D.; Chen, L.; Li, D.; Meng, S.; Chen, M. Synthesis of redox-mediator-free direct Z-scheme AgI/WO3 nanocomposite photocatalysts for the degradation of tetracycline with enhanced photocatalytic activity. *Chem. Eng. J.* **2016**, *300*, 280−290.

(53) Chen, F.; Yang, Q.; Sun, J.; Yao, F.; Wang, S.; Wang, Y.; Wang, X.; Li, X.; Niu, C.; Wang, D.; Zeng, G. Enhanced Photocatalytic Degradation of Tetracycline by AgI/BiVO4 Heterojunction under Visible-Light Irradiation: Mineralization Efficiency and Mechanism. *ACS Appl. Mater. Interfaces* **2016**, *8* (48), 32887−32900.

(54) Hao, L.; Huang, H.; Guo, Y.; Du, X.; Zhang, Y. Bismuth oxychloride homogeneous phasejunction BiOCl/Bi12O17Cl2 with unselectively efficient photocatalytic activity and mechanism insight. *Appl. Surf. Sci.* **2017**, *420*, 303−312.

(55) Cheng, H.; Wang, W.; Huang, B.; Wang, Z.; Zhan, J.; Qin, X.; Zhang, X.; Dai, Y. Tailoring AgI nanoparticles for the assembly of AgI/BiOI hierarchical hybrids with size-dependent photocatalytic activities. *J. Mater. Chem. A* **2013**, *1* (24), 7131−7136.

(56) Wang, J.; Tang, L.; Zeng, G.; Deng, Y.; Liu, Y.; Wang, L.; Zhou, Y.; Guo, Z.; Wang, J.; Zhang, C. Atomic scale g-C3N4/Bi2WO6 2D/2D heterojunction with enhanced photocatalytic degradation of ibuprofen under visible light irradiation. *Appl. Catal., B* **2017**, *209*, 285−294.

(57) Zhang, L.; Niu, C.-G.; Xie, G.; Wen, X.-J.; Zhang, X.-G.; Zeng, G. Controlled growth of BiOCl with large {010} facets for dye self-photosensitization photocatalytic fuel cells application. *ACS Sustainable Chem. Eng.* **2017**, *5*, 4619.

(58) Zhang, C.; Lai, C.; Zeng, G.; Huang, D.; Tang, L.; Yang, C.; Zhou, Y.; Qin, L.; Cheng, M. Nanoporous Au-based chronocoulometric aptasensor for amplified detection of Pb 2+ using DNAzyme modified with Au nanoparticles. *Biosens. Bioelectron.* **2016**, *81*, 61−67.

(59) Zeng, G.; Zhang, C.; Huang, D.; Lai, C.; Tang, L.; Zhou, Y.; Xu, P.; Wang, H.; Qin, L.; Cheng, M. Practical and regenerable electrochemical aptasensor based on nanoporous gold and thymine-Hg2+-thymine base pairs for Hg2+ detection. *Biosens. Bioelectron.* **2017**, *90*, 542−548.

(60) Deng, Y.; Tang, L.; Zeng, G.; Zhu, Z.; Yan, M.; Zhou, Y.; Wang, J.; Liu, Y.; Wang, J. Insight into highly efficient simultaneous photocatalytic removal of Cr(VI) and 2,4-diclorophenol under visible light irradiation by phosphorus doped porous ultrathin g-C3N4 nanosheets from aqueous media: Performance and reaction mechanism. *Appl. Catal., B* **2017**, *203*, 343−354.

(61) Guo, C.; Xu, J.; Wang, S.; Zhang, Y.; He, Y.; Li, X. Photodegradation of sulfamethazine in an aqueous solution by a bismuth molybdate photocatalyst. *Catal. Sci. Technol.* **2013**, *3* (6), 1603.

(62) Dong, F.; Li, C.; He, G.; Chen, X.; Mao, X. Kinetics and degradation pathway of sulfamethazine chlorination in pilot-scale water distribution systems. *Chem. Eng. J.* **2017**, *321*, 521−532.

(63) Chen, F.; Yang, Q.; Li, X.; Zeng, G.; Wang, D.; Niu, C.; Zhao, J.; An, H.; Xie, T.; Deng, Y. Hierarchical assembly of graphene-bridged $Ag_3PO_4/Ag/BiVO_4$ (040) Z-scheme photocatalyst: An efficient, sustainable and heterogeneous catalyst with enhanced visible-light photoactivity towards tetracycline degradation under visible light irradiation. *Appl. Catal., B* **2017**, *200*, 330−342.

(64) Chen, F.; Yang, Q.; Wang, S.; Yao, F.; Sun, J.; Wang, Y.; Zhang, C.; Li, X.; Niu, C.; Wang, D.; Zeng, G. Graphene oxide and carbon nitride nanosheets co-modified silver chromate nanoparticles with enhanced visible-light photoactivity and anti-photocorrosion properties towards multiple refractory pollutants degradation. *Appl. Catal., B* **2017**, *209*, 493−505.

(65) Cheng, M.; Zeng, G.; Huang, D.; Lai, C.; Liu, Y.; Xu, P.; Zhang, C.; Wan, J.; Hu, L.; Xiong, W.; et al. Salicylic acid−methanol modified steel converter slag as heterogeneous Fenton-like catalyst for enhanced degradation of alachlor. *Chem. Eng. J.* **2017**, *327*, 686−693.

(66) Chen, F.; Yang, Q.; Zhong, Y.; An, H.; Zhao, J.; Xie, T.; Xu, Q.; Li, X.; Wang, D.; Zeng, G. Photo-reduction of bromate in drinking water by metallic Ag and reduced graphene oxide (RGO) jointly modified BiVO 4 under visible light irradiation. *Water Res.* **2016**, *101*, 555−563.

(67) Deng, Y.; Tang, L.; Zeng, G.; Feng, C.; Dong, H.; Wang, J.; Feng, H.; Liu, Y.; Zhou, Y.; Pang, Y. Plasmonic resonance excited dual Z-scheme BiVO4/Ag/Cu2O nanocomposite: synthesis and mechanism for enhanced photocatalytic performance in recalcitrant antibiotic degradation. *Environ. Sci.: Nano* **2017**, *4*, 1494.

(68) Tian, N.; Zhang, Y.; Li, X.; Xiao, K.; Du, X.; Dong, F.; Waterhouse, G. I. N.; Zhang, T.; Huang, H. Precursor-reforming protocol to 3D mesoporous g-C_3N_4 established by ultrathin self-doped nanosheets for superior hydrogen evolution. *Nano Energy* **2017**, *38*, 72−81.